

# All-Integrated Bifunctional Separator for Li Dendrite Detection via Novel Solution Synthesis of a Thermostable Polyimide Separator

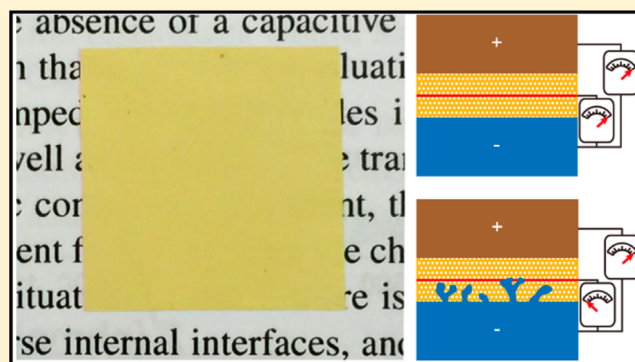
Dingchang Lin,<sup>†</sup> Denys Zhuo,<sup>†</sup> Yayuan Liu,<sup>†</sup> and Yi Cui<sup>\*,†,‡</sup>

<sup>†</sup>Department of Materials Science and Engineering, Stanford University, Stanford, California 94305, United States

<sup>‡</sup>Stanford Institute for Materials and Energy Sciences, SLAC National Accelerator Laboratory, 2575 Sand Hill Road, Menlo Park, California 94025, United States

**S** Supporting Information

**ABSTRACT:** Safe operation is crucial for lithium (Li) batteries, and therefore, developing separators with dendrite-detection function is of great scientific and technological interest. However, challenges have been encountered when integrating the function into commercial polyolefin separators. Among all polymer candidates, polyimides (PIs) are prominent due to their good thermal/mechanical stability and electrolyte wettability. Nevertheless, it is still a challenge to efficiently synthesize PI separators, let alone integrate additional functions. In this work, a novel yet facile solution synthesis was developed to fabricate a nanoporous PI separator. Specifically, recyclable LiBr was utilized as the template for nanopores creation while the polymer was processed at the intermediate stage. This method proves not only to be a facile synthesis with basic lab facility but also to have promising potential for low-cost industrial production. The as-synthesized PI separator exhibited excellent thermal/mechanical stability and electrolyte wettability, the latter of which further improves the ionic conductivity and thus battery rate capability. Notably, stable full-cell cycling for over 200 cycles with a PI separator was further achieved. Based on this method, the fabrication of an all-integrated PI/Cu/PI bifunctional separator for dendrite detection can be fulfilled. The as-fabricated all-integrated separators prove efficient as early alarms of Li penetration, opening up the opportunity for safer battery design by separator engineering.



## INTRODUCTION

High-energy/power-density energy storage devices are of increasing demand for portable electronics and electric vehicle applications.<sup>1–3</sup> Among all the possible candidates, lithium (Li) batteries have been garnering the most attention due to their outstanding performance. In the past several decades, various anode materials, including Si,<sup>4–7</sup> Ge,<sup>8</sup> Sn,<sup>9,10</sup> and ultimately Li metal,<sup>11–16</sup> have been extensively studied for next-generation high-energy-density Li battery anodes in succession to the conventional graphite. However, for all the above-mentioned anodes, safety remains a concern.<sup>17</sup> Even with commercial graphite, which is known as a relatively safe Li<sup>+</sup> host, dendritic Li metal can still be plated out, especially when cycled at elevated current densities, low temperatures, or overcharge conditions.<sup>18–21</sup> The plated Li dendrite can penetrate through the separator and initiate intense heat release via internal short circuit, which will further bring about thermal runaway and a potential explosion hazard.<sup>21,22</sup> The issue is even more severe for high-energy-density anodes such as Li metal, whose “hostless” nature can trigger uncontrollable dendritic Li plating even at relatively low current densities.<sup>11,23</sup>

Recently, an extensive study has been carried out on developing advanced battery separators.<sup>24</sup> On the one hand, advanced nanotechnology, such as self-assembly<sup>25,26</sup> and

electrospinning,<sup>27–29</sup> was developed for fabricating separators. On the other hand, high-strength materials, such as aramid and polyoxazole, were applied to suppress dendrite penetration.<sup>30,31</sup> However, to safely operate batteries in diversified environments and situations, an early alarm of dendrite penetration is strongly desired. It has been reported that incorporating a metallic detection layer in between two commercial separator layers is valid to sense Li dendrite penetration.<sup>32</sup> By measuring the potential between the metallic interlayer and the negative electrode, dendrite penetration can be efficiently detected from a sudden voltage drop, which alarms the upcoming internal short circuit and the necessity of disposing of the problematic cells. Nevertheless, utilizing two separate layers of separator is not practical in real applications due to the increased internal resistance from the additional layer and the associated engineering challenges during cell assembling.<sup>32</sup> Thus, an all-integrated separator needs to be developed.

However, the incorporation of Cu into polyolefin separators with commercial dry/wet processes is technically difficult, since the final pore formation/expansion step via stretching will damage the Cu interlayer. Before integrating the dendrite-

Received: June 24, 2016

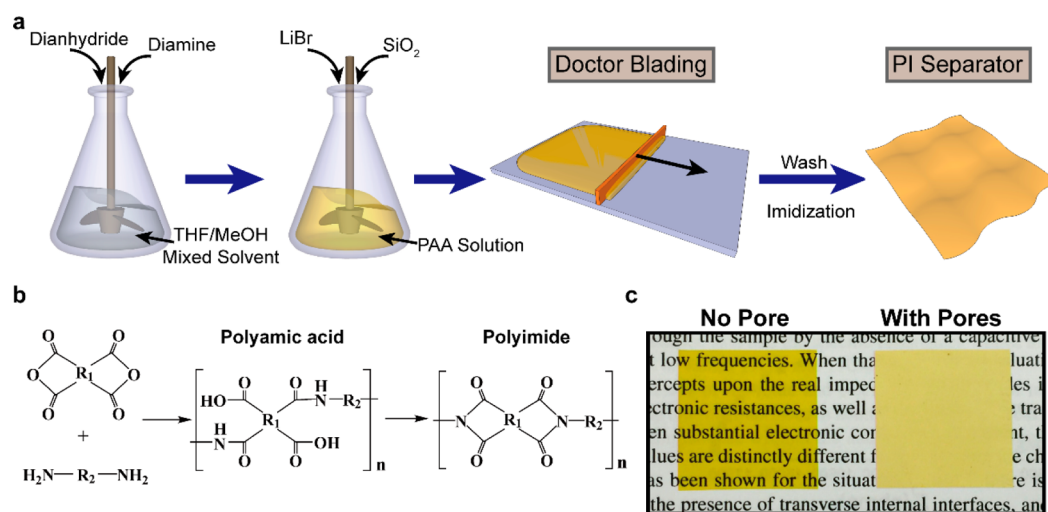


**Figure 1.** | Synthesis of the PI nanoporous membrane. (a) Synthetic procedure of the PI nanoporous membrane with LiBr salt as template. The general condensation polymerization of dianhydride and diamine for PI synthesis is shown in part b. (c) Comparison of the as-obtained membranes without pores and with pores, which were synthesized without and with the addition of LiBr salt, respectively.

detection function, we first developed a promising solution synthesis of a thermostable polyimide (PI) separator without a stretching process. Compared with commercial polyolefin separator,<sup>33,34</sup> PI is widely regarded as a promising alternative due to its excellent thermal stability, high tensile strength, and good electrolyte wettability.<sup>27,35</sup> Unfortunately, commercializing PI separator has been stagnant for decades due to grand challenges in processing.<sup>36,37</sup> Therefore, few PI separators are commercially available, while most of them are nonwoven, which is believed to be inferior to the widely used nanoporous membranes in terms of uniformity and mechanical strength.<sup>27,28,33</sup>

Herein, in order to obtain nanoporous PI separators, the fabrication was carried out at the intermediate polyamic acid (PAA) stage of the PI, which affords much better processability. LiBr salt was developed as the template, with which uniform nanopores can be created by simply removing LiBr in the H<sub>2</sub>O bath. Once dissolved, LiBr can be further recycled, and no stretching is needed during the fabrication. This simple synthesis offers an exciting possibility for a PI separator in research laboratories and potential low-cost manufacturing in industry. Noticeably, the obtained PI separator exhibited excellent thermal stability, electrolyte wettability, and mechanical stability, together with further improved ionic conductivity and, thus, rate capability. Furthermore, solution synthesis enables the fabrication of an all-integrated PI/Cu/PI trilayer bifunctional separator by sequential coating. Since no horizontal stretching is applied during the process, the incorporated Cu can remain intact when a top layer is coated. Our method also guarantees good adhesion at the interfaces of the trilayer structure. With the above merits, the as-obtained all-integrated trilayer separator was demonstrated to afford efficient dendrite-detection function.

## RESULTS AND DISCUSSION

**Solution Synthesis of Polyimide Separators.** Figure 1a schematically shows the solution synthesis procedures of the PI separator. First of all, tetrahydrofuran (THF) and methanol (MeOH) are mixed in a 4:1 volume ratio as the solvent for the condensation polymerization of the PI intermediate, polyamic acid (PAA).<sup>38,39</sup> Then, diamine and dianhydride are added

sequentially in a 1:1.02 molar ratio with vigorous stirring. The polymerization is initiated immediately once dianhydride is added, with dramatically increased viscosity as an indicator of the rapidly growing polymer chains. Note that 2 mol % more dianhydride than the stoichiometric ratio was added here so as to yield high molecular weight PI.<sup>36,37</sup> The usage of the solvent here is crucial. In contrast to the conventional solvents, such as dimethylacetamide (DMAC) and dimethylformamide (DMF) for PAA synthesis, the THF/MeOH mixed solvent affords much lower boiling point. As schematically indicated in Figure S1, since the dissolved LiBr will spontaneously adsorb the moisture from the air to help solidify the PAA, the solvent needs to be evaporated fast enough before the adsorption of a large amount of H<sub>2</sub>O in order to yield a porous membrane (Figure S1a). If solvents with high boiling point (higher than H<sub>2</sub>O) were used, as shown in Figure S1b, a large amount of H<sub>2</sub>O would be adsorbed without the removal of the solvents. As a result, PAA will precipitate into powder form rather than the porous membrane. For THF/MeOH mixed solvent, the boiling point is far lower than that of H<sub>2</sub>O, which guarantees fast evaporation of the solvent before the adsorption of a considerable amount of H<sub>2</sub>O, and thus affords a porous membrane.

Afterward, ~14 nm of fumed SiO<sub>2</sub> was added to the PAA solution, followed by the addition of LiBr as the template for later pore formation. The addition of SiO<sub>2</sub> offers several advantages: (i) SiO<sub>2</sub> can further improve the electrolyte wettability of the separator; (ii) better thermal stability and mechanical properties can be expected with the addition of ceramic fillers; (iii) it is experimentally observed that the addition of SiO<sub>2</sub> can create a more uniform pore distribution. The choice of LiBr is subtle and critical here. First of all, as mentioned above, during the solvent drying process, LiBr can adsorb moisture from the air, which can help solidify the PAA to afford porous membranes. Second, the solubility of LiBr in THF/MeOH mixed solution is extremely high so that we are able to achieve high porosity with LiBr as the template. After over 8 h of vigorous stirring, the solution was coated onto a glass substrate by doctor blading. Once the coated films were dried, they were washed with deionized (DI) water to remove LiBr and then fully dried in a vacuum oven. The dried PAA film

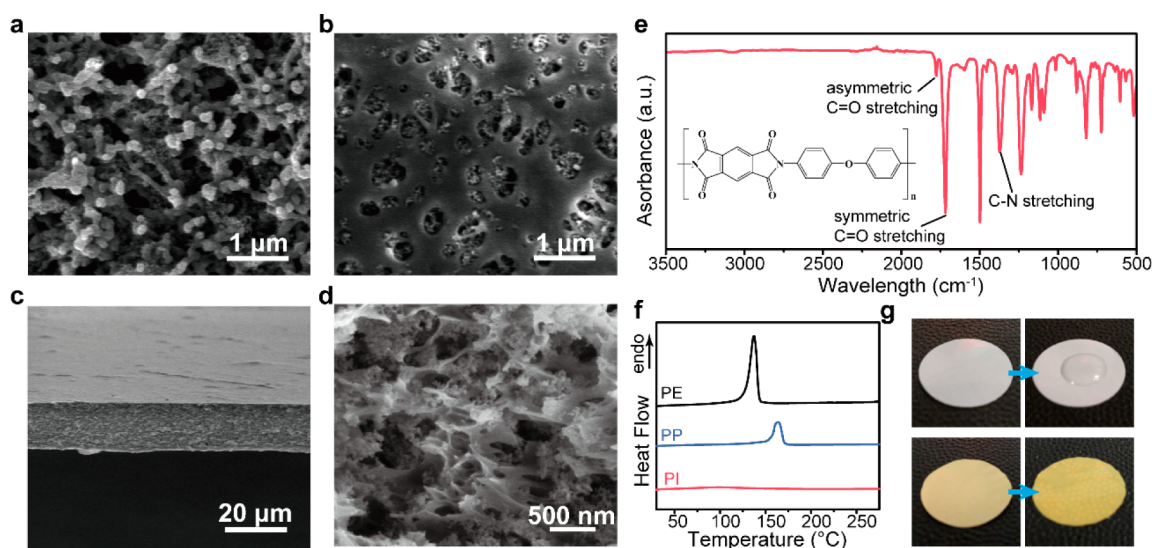


**Figure 2.** | Characterizations of the PI nanoporous membrane. (a,b) SEM images of the membrane's surface, which are the surface morphology facing air (a) and facing glass (b) in the doctor blading process, respectively. (c) Cross-section SEM image of a typical membrane showing the uniformity of the membrane thickness. (d) Magnified cross-section SEM image of a typical membrane showing the size and distribution of the nanopores. (e) FTIR spectrum of the as-obtained PI separator with PMDA and ODA as the monomers, which shows the characteristic IR absorption of PI. (f) Comparison of the DSC spectra of the PI with the PE and PP separator, while the PI separator shows excellent thermal stability at the temperature range from 30 to 275 °C. (g) Digital camera photos comparing the wettability of a commercial separator and the as-synthesized PI separator with a propylene carbonate electrolyte.

was finally imidized in air at 300 °C to yield the imide rings. The overall chemical reactions are shown in Figure 1b, where the first step is to form the PAA intermediate and the second step is fulfilled by thermal imidization. The  $R_1$  and  $R_2$  can be varied to form different types of PIs. A few of them were demonstrated and listed in Figure S2. The resulting PI membranes are shown in Figure 1c, where the left and right show the membranes without and with the addition of LiBr, respectively. It is clearly shown that, without LiBr template, the film exhibited clear and transparent features, while, in contrast, the addition of LiBr would yield an opaque film as the result of light scattering by nanopores. The porous membrane also appears quite uniform without any obvious defect from visual inspection, indicating the capability of the as-developed synthetic method for the fabrication of uniform separators.

**Characterization of the Polyimide Separators.** Detailed characterizations on the nanoporous PI separators were further carried out using scanning electron microscopy (SEM). Figure 2a, b show the surface morphologies of the PI separators on the air-facing and substrate-facing sides, respectively. Although the surface morphologies are different on the two sides, the pore sizes are all in the submicron range and well-distributed at the surface, similar to that of the typical commercial nanoporous separator fabricated by either a dry or wet process.<sup>33</sup> To observe the overall film uniformity and pore-size distribution inside the film, the low-magnification and magnified cross-section SEM images are taken and shown in Figure 2c, d, respectively. It can be clearly seen from Figure 2c that the typical  $\sim 15\text{-}\mu\text{m}$ -thick PI separator exhibited excellent uniformity with constant thickness and smooth surface. Neither large pores nor pinholes can be observed inside the separator. It is noted that, by applying doctor blading with various gap depths, the thickness of the film can be easily tuned. As shown in Figure S3, PI separators with various thicknesses from  $\sim 10\ \mu\text{m}$  to  $\sim 25\ \mu\text{m}$  can be easily fabricated, which covers the major thickness range of commercial separators. The size distribution

of the nanopores inside the film can be clearly seen from the magnified SEM image in Figure 2d. As is shown, bigger pores with the size  $\sim 200\ \text{nm}$  are interconnected by smaller pores ( $< 100\ \text{nm}$ ) and  $\text{SiO}_2$  nanoparticles are well dispersed inside the nanopores, performing as part of the skeleton and to preserve the soaked-in organic electrolyte. To verify that the as-fabricated separator was made of a PI skeleton, Fourier transform infrared spectroscopy (FTIR) was carried out and analyzed. Figure 2e shows the typical FTIR spectrum of the PI separator with pyromellitic dianhydride (PMDA) and 4,4'-oxydianiline (ODA) as the monomers, where strong characteristic symmetric C=O stretching and C–N stretching signals of PI can be identified at  $\sim 1717.99\ \text{cm}^{-1}$  and  $\sim 1369.50\ \text{cm}^{-1}$ , respectively. All the peaks well match with the typical PMDA-ODA PIs reported elsewhere,<sup>40</sup> which confirms the chemical composition of the synthesized PI separator.

Thermal stability is a critical parameter of a separator. A low melting temperature of a separator can give rise to severe separator shrinkage in the early stage of internal short circuit, which may accelerate the thermal runaway process. Conventional polyolefin separators generally have a relatively low melting point of 120–160 °C,<sup>33,34</sup> which is not high enough to sustain a stable dimension while encountering overheating. However, the PI separator is well-known for its excellent thermal stability. As indicated in the differential scanning calorimetry analysis (DSC, Figure 2f), no endothermic peak corresponding to polymer melting can be observed for the PI separator in the whole scanning range, while both polyethylene (PE) and polypropylene (PP) separators showed a strong endothermic peak at  $\sim 140\ \text{°C}$  and  $\sim 160\ \text{°C}$ , respectively. The thermogravimetric analysis (TGA) further supports the thermal stability of the PI separator (Figure S5), where the PI separator maintained its stability without weight loss up to  $\sim 400\ \text{°C}$  in both  $\text{N}_2$  and air atmosphere, outperforming the conventional PP separator, which started losing weight at  $\sim 230\ \text{°C}$  in air.

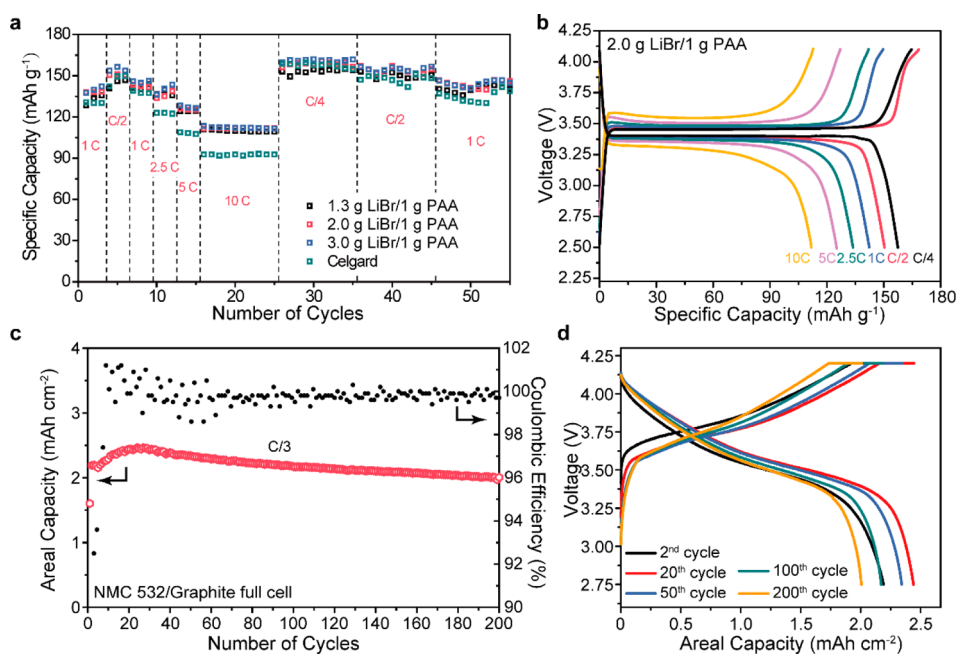


**Figure 3.** | Electrochemical performance of the PI separator. (a) Rate capability of the PI separators with different amounts of LiBr salt template and their comparison to a commercial Celgard separator. (b) Voltage profiles of the PI separator with 2.0 g LiBr/1 g PAA at various rates from C/4 to 10 C. (c) Cycling stability and Coulombic efficiency of the NMC 532/PI separator/graphite full cell with commercial level areal capacity. Discharge areal capacity was shown. The full cell is run at C/3. (d) Voltage profiles of the NMC 532/graphite full cell with PI separator at the 2nd, 20th, 50th, 100th, and 200th cycles.

The porosity of the PI separator was examined by a liquid absorption test, where mineral oil was used as the liquid.<sup>41</sup> The density of mineral oil is  $0.85 \text{ g cm}^{-3}$ , while the density of the PI separator's material is estimated to be  $\sim 1.67 \text{ g cm}^{-3}$  (average of 1 g of PMDA-ODA polyimide ( $1.42 \text{ g cm}^{-3}$ ) and 0.25 g of  $\text{SiO}_2$  ( $2.65 \text{ g cm}^{-3}$ )). The calculated porosity of the PI separator with 2 g of LiBr as template is  $\sim 65\%$ , which is much higher than the commercial Celgard 2400 separator, which exhibited  $\sim 42\%$  porosity in our test ( $\sim 41\%$  in the data sheet by Celgard). The Brunauer–Emmett–Teller (BET) surface area was also measured here (Figure S6), where the PI separator exhibited  $\sim 48.05 \text{ m}^2 \text{ g}^{-1}$ , higher than the Celgard 2400 counterpart ( $\sim 39.65 \text{ m}^2 \text{ g}^{-1}$ ).

Despite the high porosity, the as-synthesized PI separator still retains good mechanical strength, with a high Young's modulus of  $\sim 1 \text{ GPa}$  and high ultimate tensile strength of  $\sim 36 \text{ MPa}$  (Figure S7). For commercial dry-process polyolefin separators, although the machine direction has a high ultimate tensile strength of  $\sim 100 \text{ MPa}$ , it is actually limited by the much weaker strength along the transverse direction ( $\sim 10 \text{ MPa}$ ).<sup>33</sup> For the PI separator, since no stretching was applied throughout the synthetic processes, isotropic tensile strength can be expected, which is highly favorable for the separator. The PI separator also exhibited good flexibility, as it can be bended and twisted easily without breaking the membrane (Figure S8).

Due to the polar functional groups of PI and the uniformly embedded  $\text{SiO}_2$  nanoparticles, the as-obtained separator yields excellent electrolyte wettability. Here, 1 M  $\text{LiPF}_6$  in propylene carbonate (PC) was utilized to compare the electrolyte wettability of the commercial polyolefin separator and the PI separator (Figure 2g, Movie S1). According to Figure 2g, the PC electrolyte dropped on the commercial Celgard PP/PE/PP separator maintained as a droplet and cannot be well absorbed into the separator (top photos, left and right, are before and after adding electrolyte, respectively), while the PI separator

exhibited highly improved electrolyte absorption where the electrolyte can promptly diffuse across the whole area (bottom photos, left and right, are before and after adding electrolyte, respectively). The dynamic process can be further compared in Movie S1. Besides, commercial carbonate electrolyte of 1 M  $\text{LiPF}_6$  in 50/50 (v/v) ethylene carbonate (EC)/ diethyl carbonate (DEC) was also used for comparison (Figure S9), where PI separator also exhibited much better electrolyte wettability.

**Rate Capability and Full-Cell Cycling Stability.** The excellent wettability enables highly improved battery rate capability. For fair comparison,  $25 \mu\text{m}$  of PI separator, which has the same thickness as the commercial separators, was fabricated and used to characterize the electrochemical performance.  $\text{LiFePO}_4$  (LFP) and Li foil were used as the cathode and anode, respectively. PI separators made with the addition and dissolution of different amounts of LiBr template, varied from 1.3 to 3.0 g (/1 g PAA), were tested here. As shown in Figure 3a, all three PI separators with various amounts of LiBr addition showed better rate capability compared with commercial Celgard 2325 separator, especially at high rate. Among the three different PI separators, 2.0 and 3.0 g LiBr (/1 g PAA) show slightly higher capacity retention, which indicates that the addition of 2.0 g LiBr (/1 g PAA) is enough to create sufficient porosity for good kinetics. The voltage profiles at different rates from C/4 to 10 C of a typical PI separator (2.0 g LiBr/1 g PAA) are shown in Figure 3b, where lower charge/discharge hysteresis ( $\sim 240 \text{ mV}$ ) than that of the commercial Celgard separator (Figure S10) can be observed at a high rate of 10 C, with  $>110 \text{ mAh g}^{-1}$  of capacity retention. The AC impedance spectroscopy measurement further supports the better kinetics of the PI separator (Figure S11). As is shown, the PI separators consistently have lower resistance than the commercial Celgard 2325 separator.

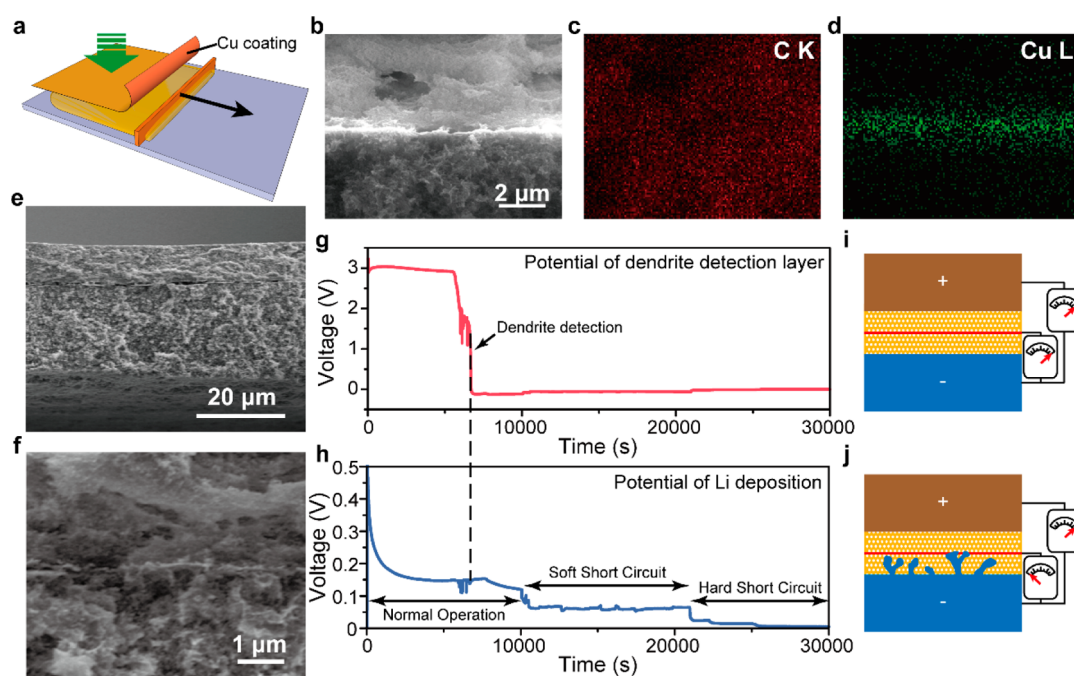


**Figure 4.** | All-integrated PI/Cu/PI trilayer bifunctional separator and Li dendrite detection. (a) Schematic illustration of the major fabrication process of the all-integrated PI/Cu/PI trilayer bifunctional separator. A Cu-coated PI separator is adhered to a fresh wet surface during the ongoing doctor blading process, with the Cu-coated surface facing down. (b–d) C K (c) and Cu L (d) EDX mapping signals of the trilayer interface shown in part b. A Cu interlayer can be clearly detected. (e) Low-magnification cross-section SEM images showing the uniformity of the trilayer structure. (f) Magnified cross-section SEM images showing the trilayer interface with the Cu layer in the middle. (g) Obtained voltage profile when monitoring the Cu layer versus  $\text{Li}^+/\text{Li}$  ( $V_{\text{Cu-Li}}$ ) during Li deposition onto the negative electrode. (h) Obtained voltage profile ( $V_{\text{Li-Li}}$ ) of Li deposition from the positive electrode to the negative electrode. The current applied here is  $4 \text{ mA cm}^{-2}$  to accelerate the dendrite growth. The dendrite-detection mechanism is schematically showed in parts i and j, where part i shows the initial stage of Li deposition ( $V_{\text{Cu-Li}} > 0$  and  $V_{\text{Li-Li}} > 0$ ). Once Li dendrites started penetrating into the separator and touch the Cu interlayer (j),  $V_{\text{Cu-Li}}$  drops suddenly to  $\approx 0$  (corresponding to the position marked with the dashed line in parts g and h), warning of the impending failure due to internal short circuit. However, the full battery still runs safely with  $V_{\text{Li-Li}} > 0$ .

Electrochemical stability is another critical parameter for a separator. To evaluate the PI separator's electrochemical stability window, cyclic voltammetry (CV) scanning was performed within the potential range of  $-0.3$  to  $6 \text{ V}$  versus  $\text{Li}^+/\text{Li}$ , with a scan rate of  $1 \text{ mV s}^{-1}$ . As is indicated in Figure S12, the sharp peaks close to  $0 \text{ V}$  correspond to the Li plating/stripping process, while the small peak at  $\sim 4.2 \text{ V}$  can be attributed to the anodic oxidation of the liquid electrolyte. Elsewhere, no observable peak can be defined within the whole range. This is a strong demonstration that the as-fabricated PI separator has reasonable electrochemical stability for the Li-ion battery chemistry.

Furthermore, full-cell performance without excess prestored Li is the strongest evidence to prove the usefulness of a separator. In this work, matched full cells with commercial-level areal capacity ( $\sim 2.61 \text{ mAh cm}^{-2}$ ) were assembled and tested.  $\text{LiNi}_{0.5}\text{Mn}_{0.3}\text{Co}_{0.2}\text{O}_2$  (NMC 532) was used as the cathode while mesocarbon microbeads (MCMB) graphite was used as the anode. The areal capacity of the MCMB graphite anode was designed to be 10% higher in order to prevent metallic Li plating. Figure 3c shows the cycling stability and Coulombic efficiency of the NMC 532/PI separator/MCMB full cell operated at the rate of  $C/3$ . After over 200 cycles, the full cell still retained  $\sim 91.2\%$  of the initial discharge capacity (compared with the second discharge), approaching high stabilized Coulombic efficiency of  $\sim 99.9\%$ . The voltage profiles with increasing cycle numbers (Figure 3d) also show a minimal increase in voltage hysteresis, which further proves the stable

cycling of the full cell with a PI separator. After cycling in a full cell for 80 cycles (Figure S13), the separator exhibited no morphology change or mechanical failure, which supports the excellent stability of the PI separator within a cell.

**All-Integrated Bifunctional Separators and Dendrite Detection.** The proposed novel solution synthesis of a PI separator with outstanding thermal, mechanical, and electrochemical stability as well as excellent electrolyte wettability enables the fabrication of the all-integrated PI/Cu/PI trilayer bifunctional separator for the dendrite-detection application. Figure 4a schematically illustrates the major fabrication process of the all-integrated bifunctional separator. Specifically, with a PI separator fabricated by the above-mentioned method,  $\sim 50 \text{ nm}$  of Cu was sputtered on one side. Then, doctor blading was employed to coat the PAA- $\text{SiO}_2$ -LiBr precursor on a glass while at the mean time the Cu-coated PI separator was adhered to the fresh precursor surface before the film was dried. It is noted that the process needs to be carried out in a dry atmosphere, which will prevent the adsorption of moisture onto the interface and affect the interface adhesion. Once fully dried, LiBr template was washed with DI water and the separator was then dried again in vacuum oven. Finally, the imidization process was performed in argon atmosphere to prevent Cu oxidation. The as-obtained all-integrated trilayer separator exhibited robust interface adhesion. Energy-dispersive X-ray spectroscopy (EDX) mapping of C K (Figure 4c) and Cu L (Figure 4d) at the position in Figure 4b clearly shows the Cu interlayer signal sandwiched between the two PI separator

layers. The C K signal, which appears uniformly across the whole area, is attributed to the carbon-based polymeric matrix. The cross-section SEM images (Figure 4e, f) further support the good interface adhesion. In the low-magnification SEM image (Figure 4e) the trilayer structure with  $\sim 8 \mu\text{m}$  top PI layer and  $\sim 18 \mu\text{m}$  bottom layer can be clearly distinguished, and the magnified SEM image (Figure 4f) further proves the strong adhesion of the thin Cu layer in between the two PI layers. It shall be noted that a relatively thin top PI layer and a thick bottom layer were fabricated on purpose in order to make full use of the battery before alarm. If the two separator layers are of the same thickness, which is the case for the previously reported work, dendrite only grows half way into the separator when failure alarm is triggered. However, in fact, batteries can still safely run for a relatively long time before real short circuit occurs. Our design with different top/bottom layer thicknesses guarantees maximized cell operation time by only triggering alarms when the cell is approaching short circuit.

To demonstrate the dendrite-detection function of the all-integrated bifunctional separator, symmetric cells with Li foils as both electrodes are assembled in a pouch-cell configuration. A third electrode connecting the Cu layer was used for dendrite detection, and the potential of the Cu layer versus the Li negative electrode was real-time detected. Figure 4g and h show the voltage profiles of the Cu detection layer and the Li plating process, respectively, while Figure 4i and j schematically illustrate the dendrite-detection mechanism. At the initial stage before Li deposition, as indicated in Figure 4i, the Cu detection layer has a high potential,  $\sim 3 \text{ V}$  versus  $\text{Li}^+/\text{Li}$ , and remains stable (early stage in Figure 4g). After a certain time of safe operation, Li dendrites start to grow into the separator and touch the Cu layer (Figure 4j). The Li dendrites electrically connect the Cu layer and the negative electrode, which brings about the sudden drop of the detection potential from  $\sim 3 \text{ V}$  to  $\sim 0 \text{ V}$  (as marked with dashed line in Figure 4g, h). It is noted that, after the detection of dendrite, the whole cell can still operate safely for a brief period of time (Figure 4h) before soft short circuit and, later, hard short circuit occur. The results clearly demonstrate the efficient Li dendrite-detection and forewarning function of the all-integrated PI separator after sufficient cell operation time.

## CONCLUSION

In this work, we reported a novel yet facile solution synthesis for the fabrication of PI nanoporous membranes for all-integrated bifunctional Li-ion battery separator applications. By utilizing LiBr salt as the template for nanopores creation, the separator was processed at the intermediate PAA stage followed by thermal imidization. A doctor blading process was used to fabricate the separators without any stretching process. The synthetic approach not only can be performed easily with a basic lab facility but also offers great potential for commercial manufacturing. Furthermore, good electrolyte wettability, thermal stability, and mechanical strength are simultaneously achieved on the PI separator, while the good wettability further contributes to the highly improved rate capability. Notably, stable full-cell cycling with the PI separator was further achieved, which demonstrates the exciting commercialization potential of the PI separator in the Li-ion battery industry. With the solution synthesis, we are able to fabricate the all-integrated PI/Cu/PI trilayer bifunctional separator. The as-fabricated all-integrated bifunctional separator demonstrates efficient Li

dendrite detection, which sheds light on the design and fabrication of a safer battery with separator engineering.

## METHODS

**Separators Fabrication.** For the typical synthesis of PMDA-ODA separators, 2.50 mmol ( $200.2 \text{ g mol}^{-1}$ , Alfa Aesar) of ODA was first dissolved in 10 mL of THF/MeOH (4:1) solvent with vigorous mechanical stirring at  $\sim 480 \text{ rpm}$ . Then, 2.55 mmol of PMDA ( $218.12 \text{ g mol}^{-1}$ , Alfa Aesar) was slowly added into the system. The solution was kept stirring for  $\sim 2 \text{ h}$  to guarantee complete polymerization. Afterward, 0.25 g of  $\sim 14 \text{ nm}$  fumed  $\text{SiO}_2$  was added into the system, followed by the addition of LiBr (varied from 1.3 to 3 g) after  $\text{SiO}_2$  was almost uniformly dispersed. The dispersion of  $\text{SiO}_2$  takes  $\sim 2\text{--}3 \text{ h}$  with vigorous stirring. Doctor blading was applied to coat the solution into membranes with various thicknesses. After solvent evaporation, the membranes were washed with deionized  $\text{H}_2\text{O}$  and ethanol to remove LiBr. After drying the membranes under vacuum, thermal imidization was carried out with stepwise heating to  $300 \text{ }^\circ\text{C}$ . Detailed synthetic procedures of PI separators and all-integrated PI/Cu/PI trilayer separators are described in detail in the Supporting Information.

**Characterizations.** A FEI XL30 Sirion scanning electron microscope is used for SEM characterizations. Before conducting SEM study of the cycled electrodes, FTIR spectra were recorded on a Nicolet iS50 FT/IR spectrometer (Thermo Scientific). A Q2000 differential scanning calorimeter (TA Instruments) was used to conduct DSC measurements. The scanning range was from 30 to  $275 \text{ }^\circ\text{C}$  with the ramp rate  $5 \text{ }^\circ\text{C min}^{-1}$ . A Q800 dynamic mechanical analysis machine (TA Instruments) was used to conduct mechanical tests. A Q500 thermogravimetric analysis machine (TA Instruments) was utilized to carry out TGA measurements. The temperature was ramped from room temperature to  $700 \text{ }^\circ\text{C}$  with a scanning rate of  $10 \text{ }^\circ\text{C min}^{-1}$ .

**Electrochemistry.** To study the electrochemical properties of the separator, LFP/Li cells were used to analyze the rate capability while matched NMC532/MCMB full cells were used to evaluate the cycling stability. Detailed procedures for electrode fabrication and cell assembling are included in the Supporting Information. The ionic conductivity of the separator with liquid electrolyte was measured by AC impedance spectroscopy. The frequency was scanned from 1 MHz to 100 mHz. Cyclic voltammetry (CV) measurement was carried out to evaluate the electrochemical stability window, where Li foil was used as the counter electrode and a stainless steel electrode was used as the working electrode. The scanning was performed in the range  $-0.3$  to  $6 \text{ V}$  versus  $\text{Li}^+/\text{Li}$ . The scanning rate was set at  $1 \text{ mV s}^{-1}$ . A dendrite penetration test was conducted with a Li/Li symmetric cell. A high current density of  $4 \text{ mA cm}^{-2}$  was used to accelerate the Li dendrite formation and penetration. Galvanostatic cycling was conducted either on an Arbin 96-channel battery tester or on a LAND 8-channel battery tester. The AC impedance spectroscopy and CV measurements were carried out on a Biologic VMP3 system.

## ASSOCIATED CONTENT

### Supporting Information

The Supporting Information is available free of charge on the ACS Publications website at DOI: 10.1021/jacs.6b06324.

Synthesis and characterization of PI separators, mechanism for the formation of the porous membrane, structures of PIs with different dianhydrides, different thicknesses of PI separators, interfaces of the PI separators, TGA, BET surface area measurements, tensile test and flexibility of the PI separator, electrolyte wettability in EC/DEC, rate capability of the Celgard 2325 cell, ionic conductivity measurement, electrochemical stability window of the PI separator, PI separator after battery cycling, and all-integrated PI/Cu/PI trilayer bifunctional separator (PDF)

Movie showing the electrolyte wettability comparison (AVI)

## AUTHOR INFORMATION

### Corresponding Author

\*yicui@stanford.edu

### Notes

The authors declare no competing financial interest.

## REFERENCES

- (1) Tarascon, J. M.; Armand, M. *Nature* **2001**, *414*, 359.
- (2) Armand, M.; Tarascon, J. M. *Nature* **2008**, *451*, 652.
- (3) Goodenough, J. B.; Park, K.-S. *J. Am. Chem. Soc.* **2013**, *135*, 1167.
- (4) Chan, C. K.; Peng, H.; Liu, G.; McIlwrath, K.; Zhang, X. F.; Huggins, R. A.; Cui, Y. *Nat. Nanotechnol.* **2008**, *3*, 31.
- (5) Liu, N.; Lu, Z.; Zhao, J.; McDowell, M. T.; Lee, H.-W.; Zhao, W.; Cui, Y. *Nat. Nanotechnol.* **2014**, *9*, 187.
- (6) Lin, D.; Lu, Z.; Hsu, P.-C.; Lee, H. R.; Liu, N.; Zhao, J.; Wang, H.; Liu, C.; Cui, Y. *Energy Environ. Sci.* **2015**, *8*, 2371.
- (7) Sun, Y.; Liu, N.; Cui, Y. *Nature Energy* **2016**, *1*, 16071.
- (8) Park, M.-H.; Cho, Y.; Kim, K.; Kim, J.; Liu, M.; Cho, J. *Angew. Chem.* **2011**, *123*, 9821.
- (9) Derrien, G.; Hassoun, J.; Panero, S.; Scrosati, B. *Adv. Mater.* **2007**, *19*, 2336.
- (10) Zhao, K.; Zhang, L.; Xia, R.; Dong, Y.; Xu, W.; Niu, C.; He, L.; Yan, M.; Qu, L.; Mai, L. *Small* **2016**, *12*, 588.
- (11) Ding, F.; Xu, W.; Graff, G. L.; Zhang, J.; Sushko, M. L.; Chen, X.; Shao, Y.; Engelhard, M. H.; Nie, Z.; Xiao, J.; Liu, X.; Sushko, P. V.; Liu, J.; Zhang, J.-G. *J. Am. Chem. Soc.* **2013**, *135*, 4450.
- (12) Zheng, G.; Lee, S. W.; Liang, Z.; Lee, H.-W.; Yan, K.; Yao, H.; Wang, H.; Li, W.; Chu, S.; Cui, Y. *Nat. Nanotechnol.* **2014**, *9*, 618.
- (13) Lin, D.; Liu, Y.; Liang, Z.; Lee, H.-W.; Sun, J.; Wang, H.; Yan, K.; Xie, J.; Cui, Y. *Nat. Nanotechnol.* **2016**, *11*, 626.
- (14) Liu, Y.; Lin, D.; Liang, Z.; Zhao, J.; Yan, K.; Cui, Y. *Nat. Commun.* **2016**, *7*, 10992.
- (15) Yang, C.-P.; Yin, Y.-X.; Zhang, S.-F.; Li, N.-W.; Guo, Y.-G. *Nat. Commun.* **2015**, *6*, 8058.
- (16) Li, N. W.; Yin, Y. X.; Yang, C. P.; Guo, Y. G. *Adv. Mater.* **2016**, *28*, 1853.
- (17) Wen, J.; Yu, Y.; Chen, C. *Mater. Express* **2012**, *2*, 197.
- (18) Kim, S. K.; Shin, B.-J.; Kim, J. H.; Ahn, S.; Lee, S.-Y. *Electrochem. Commun.* **2008**, *10*, 1625.
- (19) Ghassemi, H.; Au, M.; Chen, N.; Heiden, P. A.; Yassar, R. S. *Appl. Phys. Lett.* **2011**, *99*, 123113.
- (20) Aurbach, D.; Zinigrad, E.; Cohen, Y.; Teller, H. *Solid State Ionics* **2002**, *148*, 405.
- (21) Amine, K.; Kanno, R.; Tzeng, Y. *MRS Bull.* **2014**, *39*, 395.
- (22) Yang, H.; Bang, H.; Amine, K.; Prakash, J. *J. Electrochem. Soc.* **2005**, *152*, A73.
- (23) Xu, K. *Chem. Rev.* **2014**, *114*, 11503.
- (24) Chung, S. H.; Manthiram, A. *Adv. Funct. Mater.* **2014**, *24*, 5299.
- (25) Kim, J.-H.; Kim, J.-H.; Choi, K.-H.; Yu, H. K.; Kim, J. H.; Lee, J. S.; Lee, S.-Y. *Nano Lett.* **2014**, *14*, 4438.
- (26) Lee, J.-R.; Won, J.-H.; Kim, J. H.; Kim, K. J.; Lee, S.-Y. *J. Power Sources* **2012**, *216*, 42.
- (27) Jiang, W.; Liu, Z.; Kong, Q.; Yao, J.; Zhang, C.; Han, P.; Cui, G. *Solid State Ionics* **2013**, *232*, 44.
- (28) Miao, Y.-E.; Zhu, G.-N.; Hou, H.; Xia, Y.-Y.; Liu, T. *J. Power Sources* **2013**, *226*, 82.
- (29) Kim, J.-M.; Kim, C.; Yoo, S.; Kim, J.-H.; Kim, J.-H.; Lim, J.-M.; Park, S.; Lee, S.-Y. *J. Mater. Chem. A* **2015**, *3*, 10687.
- (30) Tung, S.-O.; Ho, S.; Yang, M.; Zhang, R.; Kotov, N. A. *Nat. Commun.* **2015**, *6*, 6152.
- (31) Hao, X.; Zhu, J.; Jiang, X.; Wu, H.; Qiao, J.; Sun, W.; Wang, Z.; Sun, K. *Nano Lett.* **2016**, *16*, 2981.
- (32) Wu, H.; Zhuo, D.; Kong, D.; Cui, Y. *Nat. Commun.* **2014**, *5*, 5193.
- (33) Arora, P.; Zhang, Z. *Chem. Rev.* **2004**, *104*, 4419.
- (34) Zhang, S. S. *J. Power Sources* **2007**, *164*, 351.
- (35) Huang, X. J. *Solid State Electrochem.* **2011**, *15*, 649.
- (36) Takekoshi, T. *Adv. Polym. Sci.* **1990**, *94*, 1.
- (37) Ghosh, M. *Polyimides: fundamentals and applications*; CRC Press: 1996.
- (38) Echigo, Y.; Iwaya, Y.; Tomioka, I.; Furukawa, M.; Okamoto, S. *Macromolecules* **1995**, *28*, 3000.
- (39) Echigo, Y.; Iwaya, Y.; Tomioka, I.; Yamada, H. *Macromolecules* **1995**, *28*, 4861.
- (40) Yang, K. S.; Edie, D. D.; Lim, D. Y.; Kim, Y. M.; Choi, Y. O. *Carbon* **2003**, *41*, 2039.
- (41) Venugopal, G.; Moore, J.; Howard, J.; Pandalwar, S. *J. Power Sources* **1999**, *77*, 34.